J Comput Aided Mol Des (2011) 25:275–291
DOI 10.1007/s10822-011-9419-z

# Modeling of the structure and interactions of the *B. anthracis* antitoxin, MoxX: deletion mutant studies highlight its modular structure and repressor function

**Nikita Chopra · Shivangi Agarwal · Shashikala Verma · Sonika Bhatnagar · Rakesh Bhatnagar**

Received: 15 July 2010 / Accepted: 7 February 2011 / Published online: 19 February 2011


**Abstract** Our previous report on *Bacillus anthracis* toxin-antitoxin module (MoxXT) identified it to be a two component system wherein, PemK-like toxin (MoxT) functions as a ribonuclease (Agarwal S et al. JBC 285:7254–7270, 2010). The labile antitoxin (MoxX) can bind to/neutralize the action of the toxin and is also a DNA-binding protein mediating autoregulation. In this study, molecular modeling of MoxX in its biologically active dimeric form was done. It was found that it contains a conserved Ribbon-Helix-Helix (RHH) motif, consistent with its DNA-binding function. The modeled MoxX monomers dimerize to form a two-stranded antiparallel ribbon, while the *C*-terminal region adopts an extended conformation. Knowledge guided protein–protein docking, molecular dynamics simulation, and energy minimization was performed to obtain the structure of the MoxXT complex, which was exploited for the de novo design of a peptide capable of binding to MoxT. It was found that the designed peptide caused a decrease in MoxX binding to MoxT by 42% at a concentration of 2 μM in vitro. We also show that MoxX mediates negative transcriptional autoregulation by binding to its own upstream DNA. The interacting regions of both MoxX and DNA were identified in order to model their complex. The repressor activity of MoxX was found to be mediated by the 16 *N*-terminal residues that contains the ribbon of the RHH motif. Based on homology with other RHH proteins and deletion mutant studies, we propose a model of the MoxX–DNA interaction, with the antiparallel $\beta$-sheet of the MoxX dimer inserted into the major groove of its cognate DNA. The structure of the complex of MoxX with MoxT and its own upstream regulatory region will facilitate design of molecules that can disrupt these interactions, a strategy for development of novel antibacterials.

**Keywords** Toxin-antitoxin complex · MoxXT · Molecular modeling · Molecular dynamics · RHH motif · Peptide design · Docking · Repressor · Deletion mutants · Antitoxin-DNA complex

**Abbreviations**

| | |
|---|---|
| TA | Toxin-antitoxin |
| RHH | Ribbon-helix-helix |
| ORF | Open reading frame |
| CD | Circular dichroism |
| aa | Amino acids |
| RFI | Relative fluorescence intensity |
| MD | Molecular dynamics |
| EM | Energy minimization |

**Electronic supplementary material** The online version of this article (doi:10.1007/s10822-011-9419-z) contains supplementary material, which is available to authorized users.

N. Chopra · S. Bhatnagar (✉)
Division of Biotechnology, Netaji Subhas Institute of Technology, Dwarka, New Delhi 110078, India
e-mail: ecc999@gmail.com

S. Agarwal · S. Verma · R. Bhatnagar (✉)
Laboratory of Molecular Biology and Genetic Engineering, School of Biotechnology, Jawaharlal Nehru University, New Delhi 110067, India
e-mail: rakeshbhatnagar@mail.jnu.ac.in

*Present Address:*
S. Agarwal
Bacterial Pathogenesis Laboratory, Department of Pathology, Tzagournis Medical Research Facility, Ohio State University, Room No: 290, 420 W, 12th Ave, Columbus, OH 43202, USA

## Introduction

Toxin–antitoxin (TA) systems, also known as suicide or addiction modules are widely distributed in bacteria [1]. These consist of a pair of genes that encode two protein components: a stable toxin and a proteolytically susceptible antitoxin that interferes with the lethal action of the toxin. The cells are said to be 'addicted' to the labile antitoxin for their survival, since its continuous de novo synthesis is essential to sequester the more stable toxin and circumvent its deleterious activity. Additionally, the antitoxin (alone or in complex with its cognate toxin) binds to the regulatory regions localized upstream of its own Open Reading Frame (ORF) in the operon and mediates transcriptional autoregulation. It has been established that TA systems find widespread occurrence on both, the extrachromosomal elements as well as chromosomes. The TA systems have been classified into several well recognized families on the basis of their sequence and structure [2].

The TA systems located on plasmids have been implicated in the post-segregational killing effect as loss of such plasmids leads to cell death [3]. However, the chromosome-encoded TA loci function as stress managers that respond to intracellular stress signals by phenotypic switching [4]. Thus, addiction modules maintain the stability of the elements on which they are borne in the host. The TA systems have also been implicated in biofilm formation, bacterial persistence during antibiotic treatment, and bacterial pathogenesis [5]. The ability of microbes to develop multidrug resistance has proved to be a nuisance in treatment of many diseases. The ubiquitous presence of TA modules in prokaryotes and absence in eukaryotes makes them attractive drug targets.

The characterization of a TA module from *Bacillus anthracis* has been reported by us recently [6]. We showed that the PemK-like toxin possessed ribonuclease activity and also established the catalytic residues of the toxin by molecular modeling and site directed mutagenesis [7]. However, we found through sequence analysis that, while the toxin has similarity to the MazF/PemK/Kid family, the antitoxin belongs to the MetJ/Arc/CopG family. It has 70% sequence similarity to YdcD but no similarity to MazE or PemI. Accordingly, we have christened this TA module as MoxXT (wherein, MoxX denotes the antitoxin and MoxT denotes the toxin). Attempts to determine the structure of MoxT, MoxX and MoxXT complex have been made. Crystallization and data collection have been performed for MoxT. However, purification and crystallization of MoxX is hampered by a low protein yield, which may be attributed to its proteolytic susceptibility [7]. Additionally, it has low solution stability as indicated by its tendency to aggregate in solution. The inherently disordered nature of MoxX may contribute to both these factors. Attempts to purify and crystallize the MoxXT complex are complicated by the existence of MoxT, MoxX, and MoxXT oligomers in multiple stoichiometries in solution, which makes chromatographic separation difficult. Thus, homogeneous MoxXT required for crystallization is difficult to obtain. Therefore, we undertook the modeling of the MoxXT complex.

At present, the solution structure of two RHH motif containing antitoxins has been determined, namely, CcdA [8] and ParD [9]. Both the structures consist of a dimeric antitoxin with an *N*-terminal RHH domain and an extended *C*-terminal. The crystal structures of several other RHH motif containing transcriptional repressors have also been elucidated [10–13]. The crystal structure of a TA complex with a PemK-like toxin has been reported for *E. coli* MazEF [14]. The structure of *C*-terminal of CcdA in complex with its toxin CcdB is also known [8]. In both the known structures, *C*-terminal of the antitoxin is involved in binding to the toxin. In this paper, we have carried out the homology modeling of the *N*-terminal domain of MoxX. We constructed deletion mutants of MoxX to determine the regions involved in its DNA and toxin binding functions. Based on the knowledge from this and previous [7] deletion mutant studies of MoxX, modeling of the MoxXT complex was carried out. We exploited our model of MoxXT complex for de novo design of a peptide capable of inhibiting MoxXT complex formation and tested it in vitro. As this would leave the toxin free to mediate its toxic effect, this designed peptide may act as a lead compound for the development of novel antibacterial therapeutics.

We have previously reported that MoxX binds to the region upstream of its ORF [6]. Several antitoxins have been found to be involved in the transcriptional autoregulation of their own operon by binding to characteristic palindromic repeats of DNA [15–18]. Therefore, we probed into the structural determinants of MoxX binding with the regulatory regions upstream of the MoxX ORF. Structure of DNA-bound antitoxin has also been elucidated for CcdA [15] as well as for other structurally similar proteins [17]. We used knowledge from these known structures, our deletion mutant studies and DNA-binding studies to model the MoxX-DNA complex. We envisage that by inhibiting the MoxX-DNA interaction, the repression mediated by MoxX would be relieved, resulting in an uncontrolled and unregulatable transcription of the operon. However the antitoxin, being more labile, will degrade faster and the toxicity of the toxin will be unleashed. This will subsequently induce programmed cell death [19]. Thus, modeling of the MoxX complex with DNA will help facilitate design of compounds that might act as novel antibacterial agents.

## Materials and methods

### Homology modeling and structural validation of MoxT dimer

Homology modeling of the MoxT dimer was performed using *B. subtilis* YdcE (PDB ID: 1NE8) [20] followed by structure validation as described previously [7].

### Circular dichroism (CD) spectroscopy of MoxT and MoxX

The recombinant MoxT (116 amino acids/aa) and MoxX (95 aa) carrying hexa-histidine tag but devoid of any extraneous amino acids were purified from the soluble and insoluble fraction, respectively, from the *E. coli* BL21 ($\lambda$DE3) crude cell lysates. The proteins were dialyzed in 5 mM Tris–HCl (pH 8.0) The Far UV CD spectra of the recombinant MoxT (150 μg/mL) and MoxX (100 μg/mL) were obtained using a J-710 JASCO spectropolarimeter (Jasco Corp.) at 25 °C using a 10 mm cell, wavelengths between 200 and 260 nm, and a scanning speed of 50 nm/min. Three spectra were accumulated for each sample, averaged and then subjected to a buffer baseline correction. The CD values in millidegrees were analyzed for the fraction of each secondary structure in both the recombinant proteins by K2d software [21].

### Loop modeling of MoxT dimer

The loop region of the modeled MoxT dimer was remodeled using Loop refinement class of Modeller [22] and validated using PROCHECK [23].

### Motif detection in MoxX

Detection of conserved sequence/structure motifs in MoxX was carried out using several different tools. This included (a) BLAST search against the CDD [24] as well as submitting the sequence to the (b) PHYRE engine [25] and (c) HHPred server [26].

### Homology modeling of MoxX

The structural alignment of MoxX to the hits as found by motif detection methods described above was inspected and edited manually in BioEdit [27]. The final alignment was used to generate a model for residues 7–49 of MoxX using Swiss Model Workspace [28]. The MoxX dimer was generated in SIB-Deepview [29] by superposition with *E.*

**Table 1** Sequence and purpose of oligonucleotides employed in the present study

| Sequence of oligonucleotide (5′–>3′) | Purpose of study |
|---|---|
| Rev GGCCCCTAAGAAAAATACACCTCCACCGTCAACTACACAC | Promoter identification |
| $AT_{300}$F GGCCGGTACCTGATTTGCTTCTTGTCATGTGAGAGAACTGTTCATTGG | |
| $AT_{250}$F GGCCGGTACCTCGTTTTTGACGAGAAGCTTTTTACTTATAG | |
| $AT_{200}$F GGCCGGTACCACGTGAATTTTGCGGAGGAACTTTCATGTTC | |
| $AT_{150}$F GGCCGGTACCAAATAAAAGAATATGAATGTTTTGTTTG | |
| $AT_{100}$F GGCCGGTACCGAATAAGGAAGTCTTTGCAACAGG | |
| $AT_{50}$F GGCCGGTACCGGTGTCATATATATATTTGGGTG | |
| delta 1-17 (F) GCCGGATCCATGGTAACGGAATTGGACGGAATTGGA | Repressor activity |
| 30/50/80 (R) GCCGTCGACTTACCCCCCGCTAACTAAGCGTTC delta 1-30 (F) GCCGGATCCAAGAATCGCCATGAACTAATTTGC | |
| delta 1-50 (F) GCCGGATCCAAGAAACGCTACCAACATGAATCAATG | |
| delta 1-80 (F) GCCGGATCCGAGTATGAAGCAGCTCATACAG | |
| R1-40/70 (F) GCCGGATCCGTGTCCGAATCAAGTGTAACTACTG | |
| R1-40 (R) GCCGTCGACTGCCTGGCAAATTAGTTCATGGCG | |
| R1-70 (R) GCCGTCGACATTAATTTTTCCCATTTCAATGTACC | |
| LP + SP (F) GTCTTGCAAATACAATGGTATTA | DNA binding-EtBr displacement assay |
| LP + SP (R) CAGAACGTTTATGTTACCATAAT | DNA binding-EtBr displacement assay |
| $NS_{DNA}$ (F) AACAACTGGCCAGGTTCCCTCGTCCCGGGT | DNA binding-EtBr displacement assay |
| $NS_{DNA}$ (R) TTGTTGACCGGTCCAAGGGAGCAGGGCCCA | DNA binding-EtBr displacement assay |

*coli* NikR (PDB ID: 2HZV) [17] and was validated using PROCHECK [23].

### Construction of deletion variants of MoxX (*N*/*C*-terminal deletions) and repressor activity

To study the modular structure of MoxX, several deletions in the protein were constructed, encompassing the *N*-terminal and *C*-terminal regions. The strategy and primers used for the study are shown in Table 1. The DNA fragments were amplified using *B. anthracis* genomic DNA. The amplified DNA fragments were restricted with *BamH* I and *Sal* I. The fragments were subsequently ligated in the *BamH* I and *Sal* I sites of pET-28a expression vector to obtain pATΔ48N, pATΔ90N, and pATΔ150N corresponding to deletion of 16, 30, and 50 amino acid residues, respectively ('*N*' denotes *N*-terminal deletions in base pairs). Similarly, deletion mutants pATΔ228C, pATΔ168C and pATΔ78C correspond to deletion of 76, 56, and 26 amino acid residues, ('*C*' denotes *C*-terminal deletions in base pairs). The recombinant constructs, pATΔ48N, pATΔ90N, and pATΔ150N (*N*-terminal deletions) and pATΔ228C, pATΔ168C, and pATΔ78C (*C*-terminal deletions) were analyzed for their expression in BL21 (λDE3) after induction with 1 mM IPTG. The authenticity of the expressed recombinant proteins was confirmed by immunoblotting with $His_6$ murine monoclonal antibody. The pATΔ48N, pATΔ90N, and pATΔ150N (*N*-terminal deletions) and pATΔ228C, pATΔ168C, and pATΔ78C (*C*-terminal deletions), constructs were cotransformed with 300 bp total upstream DNA (placZ300AT) of the addiction module, in BL21 (λDE3) cells. The selection of the transformants was maintained by including ampicillin (100 μg/mL) and kanamycin (50 μg/mL) in the growth medium. Repressor activity was indicated by the ability of construct(s) to repress the expression of β-galactosidase which was fused with the total operator of the addiction operon. Fold repression was calculated as the ratio of the specific activity of β-galactosidase observed for control (no insert, only vector) to that of the experimental (full length protein or N/C truncated protein). The data was represented as the mean of three time points in at least three independent experiments.

### Modeling of MoxXT complex

Knowledge based rigid body docking of truncated MoxX model with MoxT was carried out using GRAMMX v1.03 protein docking server [30]. This automated docking web server uses a smoothened Lennard-Jones potential on a fine grid during the global search Fast Fourier Transformation stage. This is followed by the refinement and optimization through conjugate gradient minimizations and rescoring each minimized prediction. The output file consists of 10 models ranked as the most probable prediction candidates according to the scoring function. The models were examined on the basis of surface complementarity and similarity of binding interactions to the homologous *E. coli* MazEF [14] TA system. Further, the residues 50–67 of MoxX were modeled in this model using Sybyl v6.9. An initial helical conformation was assumed in agreement with the consensus secondary structure prediction obtained from Phyre [25]. The modeled helix was oriented in a manner similar to that of the antitoxin in the MazEF complex.

### Molecular dynamics simulations and energy minimization of MoxXT complex

The MoxXT model was minimized using Sander module of Amber 9.0 [31]. Force field parameters used were taken from the ff99SB force field included in AMBER 9 Molecular Dynamics (MD) package. All the structures were solvated in an 8.0 Å octahedral layer of TIP3P water molecules and neutralized using $Cl^-$ ions. Prior to simulations, the system was subjected to several steps of Energy Minimization (EM) and relaxation. The minimizations were carried out in two steps. Firstly, EM of all water molecules and counterions was carried out in 20,000 conjugate gradient steps to remove steric clashes, while the protein was held fixed with 100 kcal/mol/Å$^2$ force. The whole system was then subjected to an unconstrained EM in 1,000 steps of steepest descent followed by 9,000 steps of conjugate gradient. The system was then heated to 300 K for 20 ps in 2 fs time step in a constant volume (NVT) setup. Equilibration at 300 K for 50 ps was then carried out in an isobaric-isothermal (NPT) setup. Long-range electrostatic interactions were treated using Particle Mesh Ewald method [32]. MD simulations were then continued in an NPT setup for 50 ps in 2 fs time step after constraining the MoxXT backbone with 10 kcal/mol/Å$^2$ force but leaving the loop region of MoxT in both the chains and the *C*-terminal region of MoxX unconstrained. The simulated model was again minimized by 1,000 steps of steepest descent and 9,000 steps of conjugate descent.

### Peptide design

The steps involved in structure based peptide design follow the sequence search method with a fixed template as described in [33]. These are as follows:

(1) The residues constituting the binding site, on the surface of the MoxT were determined from the modeled MoxXT complex.
(2) As the stretch of residues occupying site 2 in MoxT as well as MazF are helical, first a helical poly-Ala

peptide was placed at Site 2 by superposition with MoxX.

(3) Step-wise in silico mutation was done for the critical binding residues of the peptide using Sybyl 6.9 (Tripos, Inc., USA). The mutations were introduced in view of the properties of the interacting interface residues. The rotamer positions were scanned for each of the residues with simultaneous evaluation of binding energies and the peptide sequences with the lowest energies were selected.

(4) The PDB was searched using the Sybyl 6.9-Biopolymer Search Protein Database option to select those peptides that had homologous stretches in a helical conformation. The most favorable sequence with the potential to form a helix was chosen,

(5) Lastly, the minimum energy conformation of the peptide was calculated using the Pepfold server [34].

### Flexible docking of the designed peptide

For flexible docking of the peptide, the Rosetta FlexPepDock [35] protocol was employed. This method is especially suitable for obtaining high resolution models of peptide-protein complexes starting from coarse grained models. The server uses a non-biased modeling protocol that has been demonstrated to yield highly accurate models even when starting from remote structures. Two alternating modules are used to optimize the peptide backbone conformation as well as rigid body orientation using the Monte Carlo with Minimization approach. Moreover, the method has been validated over an extensive dataset of 89 different peptide-protein interactions. It can give accurate results even for long peptides with up to 60 rotatable bonds. In the present run, the starting position was obtained from the superposition of the minimum energy conformation of the free peptide with the backbone of MoxX at Site 2 in the modeled MoxXT complex. All the backbone and side chain torsions of the designed peptide except amide bonds and ring torsions were treated as flexible. In the protein, the side chains of the interface residues were treated as flexible. The complex was subjected to 2,000 independent FlexPepDock simulations allowing an exhaustive conformational search. The top scoring model was taken as the most probable docked position.

### Binding of MoxT to peptide: ELISA and Blot overlay

ELISA was performed in a 96-well microtitre plate by coating 100 ng of peptide (SKIGAWAS) in 50 mM sodium carbonate buffer, pH 9.5 for overnight at 4 °C. The wells were then washed using 1× Phosphate buffer saline with 0.1% Tween-20 (PBST) and blocked with 100 μL of 2% SM-PBST (skimmed milk in PBST) for 2 h at 37 °C. Increasing concentrations (5 μg–80 ng) of MoxT in PBST were added and incubated for 2 h at 37 °C followed by washing with PBST for 3 min twice. The wells were then incubated with 1:5000 dilution of polyclonal anti-MoxT IgG for 1 h at 37 °C followed by washing with PBST for 3 min twice and addition of 1:10000 dilution of horseradish peroxidase conjugated goat anti-mouse IgG for 1 h at 37 °C. The color was developed by adding tetramethylbenzidine as substrate to the wells. The absorbance was measured at 630 nm in the microtitre plate ELISA reader (Tecan).

Blot immunoassay was performed by resolving 10 μg of the peptide and BSA as a nonspecific protein on a 12% SDS-PAGE and subsequently transblotted onto the nitrocellulose membrane. The blot was overlaid with 50 μg/mL of MoxT in 1× PBS followed by the addition of mouse polyclonal anti-MoxT IgG (1:5000). The blot was then incubated with goat antimouse IgG-alkaline phosphatase conjugated secondary antibody (1:10000). The immunoreactive bands were visualized by adding NBT/BCIP as a substrate solution.

### Activity testing of the designed peptide

ELISA was performed by coating the wells with rMoxX followed by addition of preformed rMoxT-peptide complex, as per our previously established protocol [7]. The decrease in binding of the rMoxT-peptide to the bait protein (rMoxX) was studied by employing anti-rMoxT antiserum.

### Electrophoretic mobility shift assay (EMSA) to determine the binding of TA proteins to the upstream DNA fragment(s)

The 300 bp DNA fragment upstream of the antitoxin ORF was PCR amplified from the genomic DNA of *B. anthracis* for gel retardation assay. The PCR amplified products were end-labeled with [$\gamma^{32}$P] ATP using T4 kinase and were gel purified. Binding reaction was performed by incubating purified rMoxX (0.5, 1.0, 1.5 and 2 μM)/MoxXT complex (rMoxX: 0.5, 1.0, 1.5, and 2 μM and rMoxT: 1 μM) with radio labeled DNA (1 ng) in binding buffer (25 mM Tris–HCl, 10 mM $MgCl_2$, 50 mM NaCl, pH 7.5) and varying amounts of fragmented single stranded DNA was added in a total reaction volume of 30 μL, at 16 °C for 30 min. The products were separated on a 4% native PAG and exposed to film (X-Omat Blue XB1, Kodak) at −80 °C.

### Fluorescence spectroscopy—ethidium bromide displacement (EtBr) assay

Binding of the rMoxX to palindromes located in the upstream region was determined by ethidium bromide

displacement assay. An aqueous solution containing 10 μM DNA was titrated with increasing concentrations of EtBr. The EtBr concentration at which further increase in the fluorescence was not observed was used for all fluorescence assays. The fluorescence intensity was measured on a Cary Varian Spectrofluorimeter equipped with an external cryostatted thermal controller. Fluorescence of ethidium bromide was measured by exciting the sample at a wavelength of 520 nm and emission was recorded from 530 to 600 nm. Fluorescence quenching of DNA due to the displacement of ethidium bromide upon interaction with the protein is a direct measure of the interaction. The relative fluorescence intensity quenched was plotted against the wavelength, which was used to determine the apparent DNA binding.

### Construction of chimeric reporter (*lacZ*) fragments and β-galactosidase assay

To determine the promoter region upstream of the MoxXT locus, *lacZ* transcriptional fusions were constructed. Six constructs covering different upstream regions of the *moxX* open reading frame were PCR amplified employing *B. anthracis* genomic DNA as the template and oligonucleotides enlisted in Table 1. The amplified fragments were digested and subsequently ligated to the *BamH* I and *Kpn* I digested *pLacZ*, a promoterless vector (a kind gift from Dr. Nirupama Banerjee, ICGEB, India) to obtain *lacZ* transcriptional fusions for the detection of promoter activity. *E. coli* DH5α was transformed with the recombinant plasmids (*moxX* upstream deletion variants) and transformants were assayed for the β-galactosidase activity (when O.D. reached 0.5) according to the method of Miller [36]. The expression of β-galactosidase for each construct was reported as miller units, which are, 1000 × (Absorbance at 420 nm)/(Absorbance at 595 nm) × Time (min) × Volume (mL).

### Modeling of DNA and MoxX-DNA complex

The DNA region recognized by MoxX was inferred by similarity to other RHH binding motifs as observed in CcdA [15], RelB [16] and NikR [17]. The sequence motifs were searched for in the upstream region of the operon experimentally demonstrated to contain the promoter. The region of DNA spanning the repeats was modeled using the 3D-DART server [37] on the basis of the NMR structure of DNA in CcdA-operator complex [15] (PDB ID:2H3A). Thereafter, the MoxX-DNA complex was constructed by superposition of the obtained MoxX model and DNA model on NikR-DNA complex (PDB ID: 2HZV) [17]. The initial complex was then subjected to MD simulations.

### MD of MoxX-DNA complex

The EM of the model was done in a similar way as MoxXT complex. The MD run was carried out in the following manner. The system was first heated to 300 K over 20 ps in an NVT setup, equilibrated at 300 K over 20 ps and the production simulation was carried out at 300 K in for 200 ps in an isobaric-isothermal NPT setup. The trajectory was calculated with a 2 fs time steps using weak constraints (10 kcal/mol/Å$^2$) on all atoms and Shake constraints on hydrogen-heavy atom bonds. EM was done on the obtained model using 500 steps of steepest descent followed by 500 steps of conjugate descent.

## Results and discussion

### Antitoxin-free MoxT dimer has a ribonuclease fold and a closed loop conformation that precludes MoxX binding

The MoxT monomer forms a single globular domain consisting of three α-helices and seven β-strands as is also evident in the crystal structure of YdcE of *B.subtilis* [20]. The two structures superimposed with a very low rmsd of 0.1 Å for 116 $C_\alpha$ atoms. The monomeric MoxT has the characteristic SH3-like barrel describing a ribonuclease fold. The strands, S1, S2, S3, S6, and S7, form one antiparallel β-sheet while S4 and S5 are involved in formation of another, smaller antiparallel β-sheet. MoxT also superimposed well with the MazF toxin (rmsd of 1.5 Å in 162 structurally equivalent $C_\alpha$ atoms). The overall fold, secondary structural elements and superposition of the modeled MoxT dimer with MazF are shown in Fig. 1.

Upon formation of MoxT dimer, there are intimate hydrophobic contacts between the monomers involving segments of β-strand S6 and α-helices H1 and H3. The dimer has one convex surface and, another flat surface at the interface of the two monomers. The interaction of the two monomers at the convex surface is mediated by a loop between strands S1 and S2, whereas the formation of the flat surface is mediated primarily by helix H3. The surface area buried due to dimer formation is 1,706 Å$^2$. A comparison of the buried surface area due to dimerization, hydrophobic residues stabilizing dimer interactions and H-bonds in MoxT with the *B. subtilis* YdcE, is presented in Supplementary Table S1. We compared the secondary structure of the model to that obtained by CD spectroscopy. It was found that MoxT contained 20% helix and 39% sheet in the modeled structure. The experimentally obtained values by CD spectroscopy were 10% helix and 39% sheet, thus showing correspondence of the sheet content. As the model is based on the crystal structure of

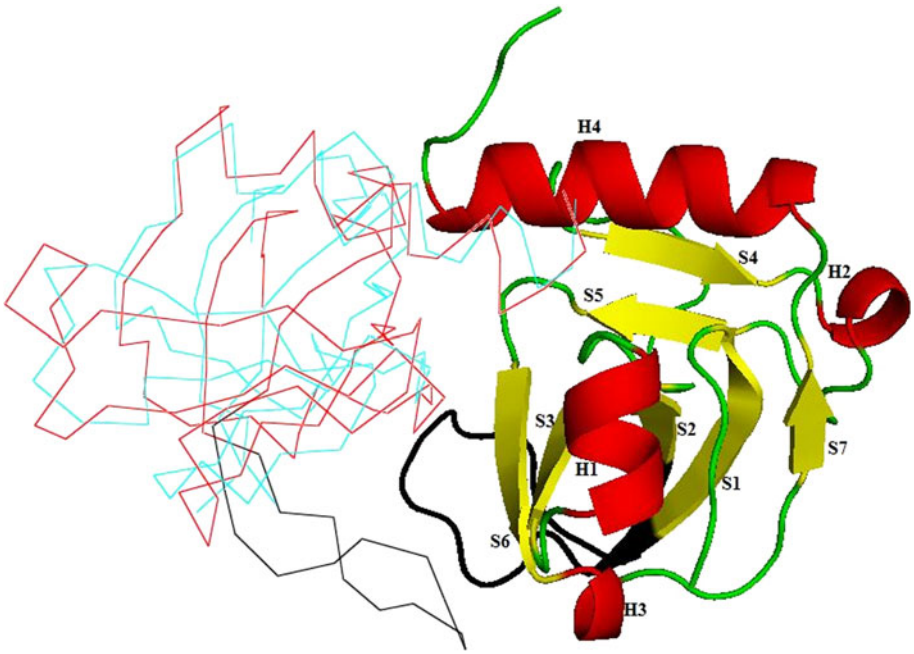


**Fig. 1** Structure of the modeled MoxT dimer. One of the chains of the monomer is shown in cartoon colored by secondary structure (*Red-helices*, *yellow sheets*, *green loops*). The secondary structural elements H1–H4 and S1–S7 are labeled for this monomer. In the other monomer, the toxin is shown as a *red* ribbon superimposed on the cyan MazF ribbon. In both monomers of the modeled toxin, residues 12–26 are shown in *black*. These residues are responsible for formation of a loop that is in closed configuration (as shown in *black*) in antitoxin-free state. The figure was rendered using Pymol

YdcE, the decrease in the helical content as determined by CD can be attributed to the partial unwinding of the *C*-terminal helix of MoxT in solution. The residues 104–116 corresponding to the terminal helix were predicted as disordered using the PredictProtein Metadisorder server [38].

Previously, it has been observed on structural comparison of the toxins of the MazF/Kid/PemK family, that the residues of S1–S2 loop are conserved in related toxins [39]. This loop is present in a closed conformation when the toxin is free but adopts a disordered open configuration, when bound to antitoxin [14]. MoxT was superimposed on *E. coli* MazEF [14] complex to infer its residues structurally equivalent to the S1–S2 loop of MazF. As the MoxT structure was modeled on the basis of *B. subtilis* YdcE alone, the loop residues extending from Ala12 to Arg26 were in a closed configuration as shown in Fig. 1. On comparison of the structure of MoxT with MazF in MazEF complex of *E. coli,* it was observed that upon complex formation with MoxX, there would be steric hinderance between the S1 and S2 loop of MoxT dimer and *C*-terminal region of MoxX. Thus, residues 12–26 of MoxT were remodeled in open conformation. Structural validation using PROCHECK [23] showed the model to be of good quality (Supplementary Table S2).

## MoxX has a conserved RHH motif at the N-terminus

Sequence analysis using three different methods showed that MoxX shared a conserved domain and aligned with transcriptional repressors of the MetJ/Arc/CopG family [13, 40, 41] (PDB ID: 2HZA, 2BJ9 and 2CAJ). All these three proteins contain an RHH motif. Three dimensional structure prediction of MoxX using Phyre also showed that MoxX contains a conserved RHH motif. The secondary structure prediction was in agreement with the presence of an extended region followed by two helices in the MoxX sequence. As the presence of the RHH motif is in agreement with the DNA-binding function of MoxX, the same was accepted.

The solution structure of another antitoxin with an RHH motif is seen in CcdA. Though the RHH motif is present in CcdA, the structure shows large deviations from other proteins of this family. Sequence analysis showed the insertion of seven residues in the loop between the two helices of the RHH motif in CcdA, leading to a different orientation of the helices in CcdA as compared to other members of this family [15]. However, this loop is absent in MoxX. We adopted a multiple template approach for modeling residues 7–49 of MoxX. The final multiple sequence alignment and secondary structure pattern with the templates used for modeling MoxX is shown in Fig. 2.

In RHH motif containing proteins, an extended region forms a two stranded ribbon upon dimerization. This ribbon inserts into the major groove of the DNA. Thus, the biologically active form of MoxX is a dimer, which was modeled by superposition of MoxX on the RHH motif of NikR dimer. The monomers superimposed with a low rmsd of 0.8 Å in 84 structurally equivalent $C_\alpha$ atoms as shown in Fig. 3. PROCHECK analysis of the MoxX dimer showed good model quality (Supplementary Table S3). A comparison of MoxX structure with ParD antitoxin (PDB ID: 2AN7) showed that its backbone closely follows the ParD

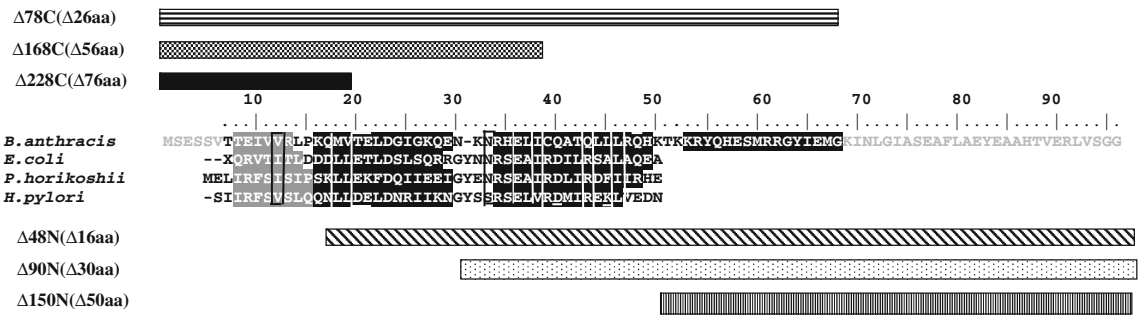


**Fig. 2** Sequence and secondary structure alignment of MoxX with known RHH motifs. Several sequence alignment programs independently detected the presence of a conserved RHH structural motif in MoxX. Alignment of the sequence with *N*-terminal domains of Nikr from *E. coli* (2HZA) and *Pyrococcus horikoshii* (2BJ9) and *Helicobacter pylori* (2CAJ) shows that the predicted secondary structural elements of the RHH motif of MoxX align well with secondary structure elements of the known crystal structures. The extended region of RHH (*shaded light grey*) and two helical stretches (*shaded black*) is shown in each of the templates. The *open boxes* indicate sequence conservation in the aligned templates. The multiple sequence alignment shown here was used to model the *N*-terminal residues 7–49 of the MoxX. The residues from 1 to 6 at the *N*-terminus and 68–95 at the *C*-terminus could not be modeled and are shown in *grey*. The span of the constructed *N*-terminal deletion mutants is shown below the sequences while the constructed *C*-terminal deletion mutants is shown above the sequences with the corresponding amino acid deletions (aa) indicated in *brackets*

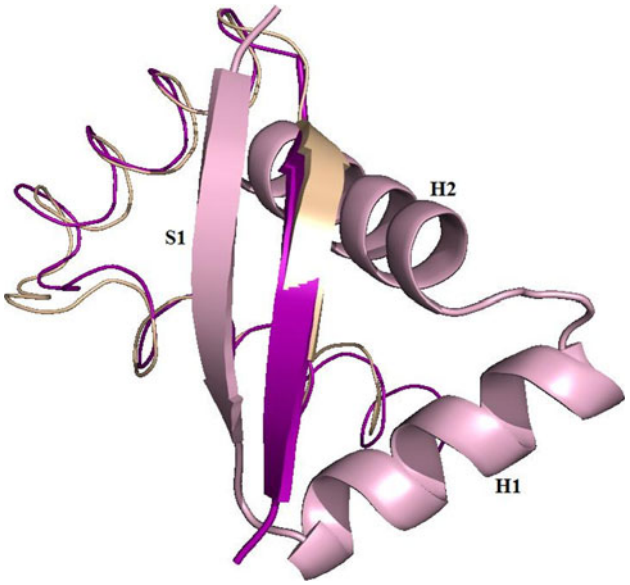


**Fig. 3** MoxX dimer showing the secondary structure elements and superposition with NikR RHH motif. The two monomers are shown in *light pink* and *purple colors*. S1, H1 and H2 correspond to the sheet and the two helices of MoxX monomer (*light pink*). The *ribbon* form of the second monomer is shown superposed on the NikR RHH motif shown in *brown* (2HZV). The two stranded $\beta$-Sheet of Nik R (*brown color*) is shown partially superposed on that of MoxX (*purple color*). The figure was rendered using Pymol

RHH structural motif. The rmsd obtained was 2.9 Å, which can be attributed to ParD being an NMR determined structure.

The MoxX model shows that the two MoxX monomers associate in a symmetrical manner via a local two-fold axis. The residues 7–49 consist of an extended region followed by two helical stretches as shown in Fig. 2. Association of the extended regions (residues 8–13) leads to the formation of a twisted antiparallel $\beta$-sheet or ribbon. The MoxX dimer is stabilized by a network of inter chain hydrogen bonds. The main chain hydrogen bonds stabilizing the ribbon formation between the two monomers include: amide of Thr8, Ile10, and Val12 (MoxXa) with carbonyl oxygens of Leu14, Val12 and Ile10 (MoxXb). Additional hydrogen bonds between the main chain and side chains that stabilize the ribbon region involve amide of Arg13 (MoxXa) with 34His-ND1 (MoxXb) and 16Lys-HZ1 (MoxXa) with 7Thr-O (MoxXb). Other main chain-side chain hydrogen bonds of the ribbon region include side chain of His34 (MoxXa) with carbonyl oxygen of Val11 (MoxXb) and side chains of Lys16 (MoxXb) with carbonyl oxygen of Thr8 (MoxXa). This ribbon, exterior to the hydrophobic core of the dimer, is responsible for interaction with the major groove of DNA, as seen in other members of MetJ/Arc/CopG family [10–18].

The solvent exposed surface area buried upon interaction of the two monomers is 1,022 Å$^2$. The hydrophobic cluster involved in dimer formation is constituted by residues of Chain A: Met18, Val19, Leu22, Ile25, Leu36 (Helix 1) and Ile37, Ala40, Thr41, Leu44, Leu45, His48 (Helix 2). In Chain B, the residues are: Met18, Leu22, Ile25 (Helix 1) and Ile37, Cys38, Ala40, Thr41, Leu44, Leu45 (Helix 2). Several inter chain salt bridges are present between His48, Lys49 and Glu29 (MoxXa) and Glu29, Glu21 and His48 (MoxXb), respectively. These salt bridges, formed between Helix 2 of the monomers, stabilize the dimer. Beyond Lys52, the unfolded MoxX main chain projects away from the other monomer making no inter chain contacts.

## MoxX has a modular structure and function: *N*-terminal RHH for transcriptional autoregulation and *C*-terminal for MoxT inhibition

To elucidate the repressor activity and modular structure of the *B. anthracis* MoxX, the full length 300 bp region immediately upstream of the *moxX* ORF in fusion with *β*-galactosidase was cotransformed with the plasmids expressing either full length or truncated MoxX. The extent of the deletions in different truncated MoxX mutants is shown in Fig. 2. The recombinant proteins were purified from the insoluble fraction employing $Ni^{+2}$-NTA chromatography to near homogeneity. The two constructs (Δ228C and Δ168C), which lacked four-fifth (80%) and three-fifth (60%) of the amino acid sequences from the *C*-terminus of the antitoxin could not be purified. This could be due to the instability associated with these small sized fragments during the purification, considering the vulnerability of antitoxin to proteases [7]. The effect of these full length/truncated variants on *β*-galactosidase expression was determined and is summarized in Table 2. The wild type protein showed a strong repression of reporter gene (244 miller units). It was observed that upon deleting the first 16 *N*-terminal amino acid residues from MoxX (Δ48n construct), the *lacZ* activity was restored (1,024 miller units) when compared to the wild type protein, which showed a strong repression of reporter gene (244 miller units) (Table 2). This clearly demonstrates the role of MoxX as a repressor of gene transcription and confirms the involvement of *N*-terminal residues in manifesting the repressor activity. It was evident from our earlier study that the *C*-terminus of MoxX exhibited MoxT binding property [7] while the *N*-terminus displayed repressor like activity proving the contention that MoxX is indeed mosaic with specialized domains for dedicated functions. The 16 amino acids at the *N*-terminus include the ribbon forming residues 8–13 of MoxX predicted to be involved in ribbon formation/DNA binding. Thus, it is confirmed that these residues have a significant role in DNA binding and imparting negative regulatory function (transcriptional repressor) to MoxX in vivo.

**Table 2** Transcriptional repressor activity of deletion mutants of MoxX

| Deletion mutant | Total miller units[a] |
|---|---|
| BL21 (*λ*DE3) | 51 |
| 300 lacZ + pET28a | 1,222 |
| 300 lacZ | 1,129 |
| 300 lacZ + 95 aa/wt | 244 |
| 300 lacZ + Δ48 N (Δ16Naa[b]) | 1,024 |
| 300 lacZ + Δ90 N (Δ30Naa) | 1,140 |
| 300 lacZ + Δ150 N (Δ50Naa) | 960 |
| 300 lacZ + Δ228C (Δ76Caa) | 745 |
| 300 lacZ + Δ168C (Δ56Caa) | 587 |
| 300 lacZ + Δ78C (Δ26Caa) | 294 |

[a] The ability of wild type MoxX and its various deletions to drive the *β*-galactosidase expression from the promoter was reported as Miller units. The values represent mean of three values obtained from three independent experiments

[b] Amino acids

On the contrary, the first *N*-terminal 20 amino acids alone (Δ228C construct) of MoxX were unable to repress the operon transcription competently, possibly due to the lack of appropriate conformation required for interaction with the promoter region. Subsequent addition of another 20 amino acids (Δ168C construct) downstream could efficiently drive significant repression implicating the role of *N*-terminal residues in governing autoregulation. Therefore, our experiments indicate that the *N*-terminal region of MoxX is involved in DNA binding and autoregulation while *C*-terminal region mediates MoxT-binding and inactivation. This supports the previous proposal that the operon itself may comprise of two evolutionarily distinct modules, namely the operator-repressor module and the antitoxin-toxin module.

## Structure of $(MoxX)_2(MoxT)_2$ complex has two conserved sites of interaction

It has been established by us earlier that the *B. anthracis* TA complex, MoxXT interacts in a molar ratio of 1:1 [7]. However, previous structural studies on toxins have established the significance of the dimer as the biologically active unit. The site for antitoxin binding lies in a cleft between the two monomers of MoxT [39]. Also, our modeling of MoxX indicates that its biologically relevant form is a dimer. Therefore, we modeled the MoxXT complex as a tetramer of two monomers of toxin and antitoxin ($A_2T_2$) each as shown in Fig. 4. In agreement with the experimental data from deletion mutants of MoxX, the interaction between MoxT and MoxX is primarily mediated by the *C*-terminus region of the MoxX [7]. It has been shown that the different toxins having the PemK fold are able to bind to antitoxins with divergent sequence and structure [42]. This is attributed to the fact that the *N*-terminal DNA-binding region of the antitoxin is minimally involved in interaction with the toxin, whereas an extended *C*-terminal region is responsible for the toxin binding. The mode of binding of antitoxin to toxin is essentially similar in the known TA complex structures. Also, two of the sites of interaction, namely, Site 1 and Site 2 are conserved [14]. In light of this, we used secondary structure prediction and the property of TA complex formation to guide the initial structure prediction for residues 50–67 of MoxX. Secondary structure prediction for these

residues was consistent with a helical conformation and they were initially modeled as a helix. Torsional angles of residues 49–52 were changed in small steps so as to allow the helix axis to be oriented similar to the *C*-terminal region of MazE bound to MazF. The results of the PROCHECK analysis were consistent with a good quality model as shown in Supplementary Table S4. MD simulations and EM were then performed on the MoxXT complex. Constraints were placed only on the backbone atoms of residues 7–49 while the side chains and residues 49–67 were allowed to move during the 50 ps simulation. The structure was then minimized with stepwise lowering of constraints in order to obtain the time averaged final structure for the flexible *C*-terminus responsible for binding to the MoxT dimer.

One MoxX chain binds between two symmetrically arranged MoxT monomers. The remaining part of the chain makes a turn and wraps around MoxT by interacting with its basic underside. The binding site for MoxX can therefore be visualized as an inverted L-shaped pocket that can also accommodate RNA as its catalytic substrate. In agreement with this, the catalytic residues His59 and Glu78 which are critically required for the ribonucleolytic activity of MoxT also lie on the surface close to the MoxX binding site as shown in Fig. 4. We also demonstrate the close

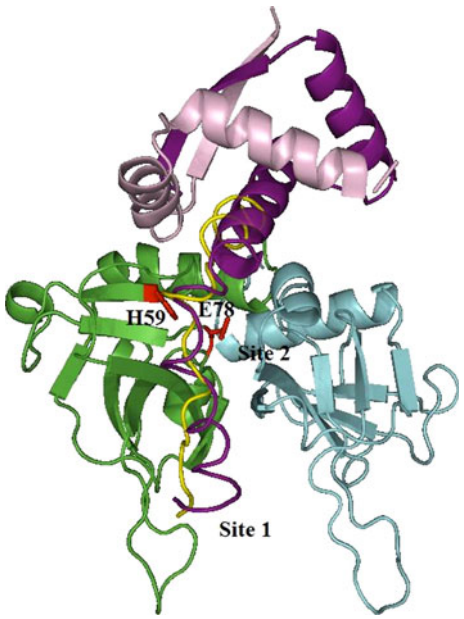


**Fig. 4** Conserved sites of interaction between MoxT toxin and MoxX antitoxin (MoxXT TA complex). The figure shows chain A (*green*) and chain B (*cyan*) of the MoxT dimer. Catalytic residues H59 and E78 as established previously by site directed mulatgenesis are shown as *red sticks*. The two MoxX monomers are shown as *light pink* and *purple*. The mode of binding of one of the monomers (*purple*) to MoxT is shown. It has been compared to MazE antitoxin of *E. coli* (*yellow ribbon*) in complex with MazF, which is structurally similar to *B. anthracis* MoxT. The conserved sites of interaction, Site 1 and 2 in are indicated. The figure was rendered using Pymol

correspondence of the *C*-terminal region of MoxX with MazE (Fig. 4) and CcdA (Supplementary figure S1). Our model of MoxXT is also consistent with its DNA-binding property as the ribbon of MoxX is free to interact with DNA even in the MoxT bound form. Comparison of secondary structure of modeled MoxX with CD spectroscopy results showed similar secondary structural content. The sheet content in the modeled structure was 7%, while helix content was 29%. The corresponding values in CD experiment were 17 and 29%. The values of the helix content matched exactly. The difference in the sheet content can be explained as follows: the MoxX model spans residues 7–67 since the entire protein could not be modeled. The additional $\beta$-sheet organization as shown by CD experiments may occur in residues 1–6 and 68–95.

Analysis of the two sites of interaction in MoxXT conserved with respect to the MazE/CcdA(*C*-terminal region)-MazF/CcdB complex showed that Site 1 is the most intimate site of interaction between MoxXT and is shown in Fig. 5a. It buries approximately 1,061 $Å^2$ solvent-accessible surface area. It consists of MoxX residues 53–61 lying in the crevice in between the two loop regions formed by toxin dimerization. A similar site of interaction in MazEF, CcdAB, and Kid/Kis complex includes a hydrophobic pocket that is occupied by Trp73 in MazE, Trp72 in CcdA, and Trp74 in Kid/Kis. The pocket is also present in MoxT dimer and is formed by Asp12, Arg25, Gln79, Arg81, and Arg87 (MoxTa) as well as Arg81, Thr82, and Ile83 (MoxTb). In our model, Tyr57 (MoxXa) lies close to this pocket. A hydrogen bond is formed by 57Tyr-OH of MoxX with 79Gln-HE2 (MoxTa) and 82Thr-O (MoxTb). As there is no tryptophan residue in MoxX, it is probable that the pocket in the MoxT is occupied by Tyr57 of MoxXa. Additional interactions stabilizing the MoxXT complex at Site 1 are provided by hydrogen bonding between 61Gly-O of MoxX with 87Arg-HH11 and 87Arg-HH2 (MoxTa) as shown in Fig. 5a.

Site 2 interactions bury 1,039 $Å^2$ solvent-accessible surface area and are shown in detail in Fig. 5b. Residues 40–41, 43–44, and 46–47 of the MoxXa chain interact with Gln50, Lys55, Leu56, His59, Glu78 (MoxTa) and with Ile34, Phe38, Ser39, Pro40, Thr41 residues (MoxTb). Extensive hydrogen bonding network is observed within this region between 49Gln-OE1, 47Arg-O, 46Lys-O, and 50His-ND1 (MoxX) with 55Lys-HZ1 (MoxTa). Hydrogen bonds are also formed by 50Gln-OE1 (MoxTa) with 50His-NE2 (MoxXa) and 39Ser-HG1 (MoxXb) with 40Arg-HE (MoxXa). This site of MoxXT interaction is also found to be conserved in other toxins of this family [14]. Additional interactions between the two components of the MoxXT complex were identified at Site 3. Residues 33–39 of MoxX make numerous contacts with Ile114 (MoxTa) and Asn32, Asp33, Ile34 (MoxTb). This interaction buries

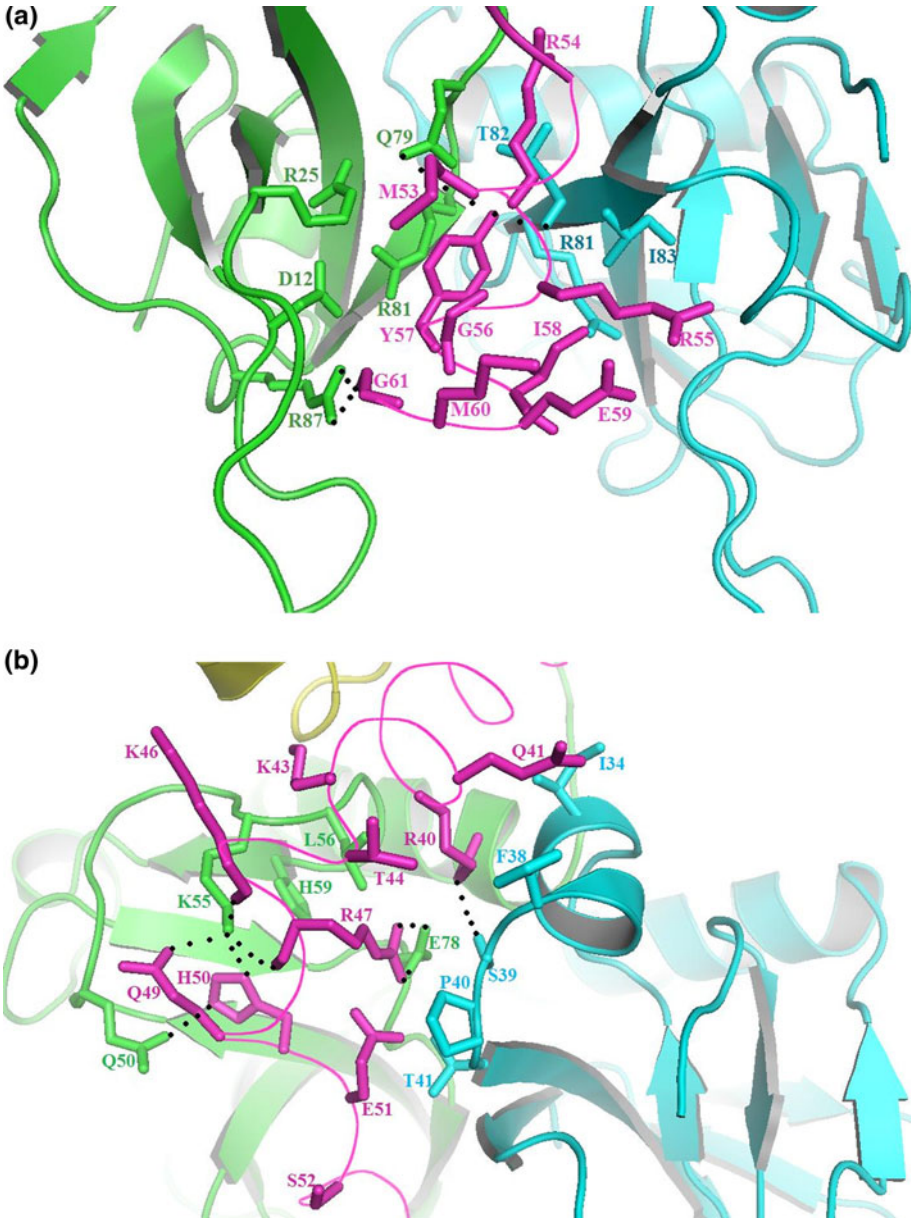


**Fig. 5** Details of interactions of MoxXT complex at the two conserved sites of interaction. **a** Site1: The residues of chain A (*green*) and chain B (*cyan*) of the MoxT dimer and the interacting residues 53–61 of MoxX (*pink*). **b** Site2: The figure shows the interacting residues of chain A (*green*) and chain B (*cyan*) of the MoxT dimer with residues 40–52 of the MoxX (*pink*). While MoxT has been rendered as a cartoon, the MoxX backbone has been rendered as a ribbon for clarity. The interacting side chains are shown as *sticks* and labeled in the corresponding color. Hydrogen bonding between MoxX and MoxT residues is depicted by *black dots*. The figure was rendered using Pymol

378 $Å^2$ of solvent-accessible molecular surface area, which is much smaller as compared to Sites 1 and 2. It is additionally stabilized by hydrogen bond formation between MoxTb 32Asn-HD11 and 36Gln-OE1 of MoxX.

We have earlier established that the deletion of 46 amino acids from the *N*-terminus lowers the ability of MoxX to bind to MoxT by 25%. In the MoxXT model, residues 40–46 of MoxX contribute to MoxT binding at Site 2. Residues 33–39 of MoxX also contribute to binding at Site 3. The deletion of 46 residues from *N*-terminus of MoxX removes its binding at Site 3 and partially interferes with binding at Site 2 of MoxT. Therefore, comparison with other known TA structures and deletion mutant studies of MoxX performed by us earlier [7] support the nature of interactions observed in the MoxXT complex.

## A rationally designed octapeptide inhibits MoxX binding to MoxT

As evident from the structural modeling of the MoxXT complex, Site 1 is formed by the juxtaposition of the disordered *C*-terminal region of MoxX with the disordered S1–S2 loop of MoxT. In contrast, Site 2 is well-ordered in both the interacting molecules. Our earlier studies have also shown that the peptides binding to Site 2 show greater efficacy in inhibiting the MoxXT interactions [7]. The region of MoxX binding to Site 2 is found to adopt a helical conformation in MoxXT as well as in MazEF. Therefore, we designed an octapeptide with the sequence SKIGAWAS, which has the potential to form α-helix and to mimic MoxX binding to Site 2 of MoxT. In its minimum energy

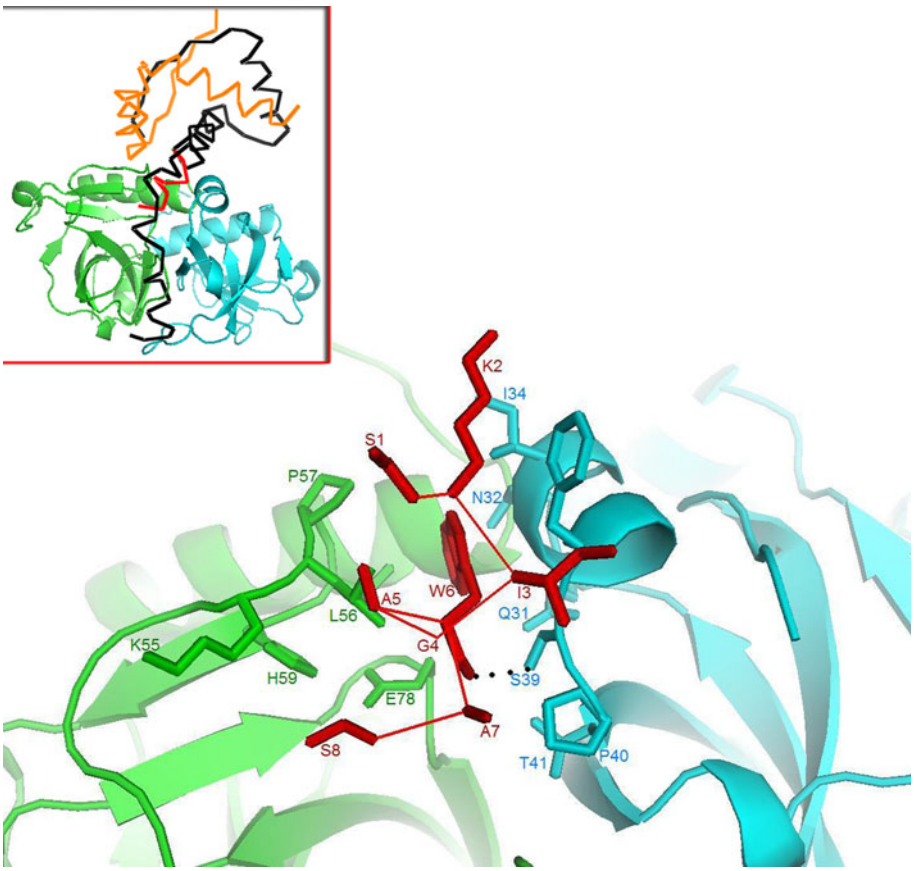


**Fig. 6** Peptide docking with the MoxT dimer. The figure shows the docked pose of the peptide (*red*) on the closed loop conformation of MoxT (*green* and *cyan* monomers). The hydrogen bonding between the residues of the peptide and MoxT is shown as *black dots*. *Inset* Backbone of the peptide is shown superposed on residues 44–49 of MoxX in MoxXT complex. The figure was rendered using Pymol

conformation, only the central residues (IGAWA) had a helical conformation while the terminal residues were partially unfolded.

The designed peptide was subjected to extensive flexible docking studies using FlexPepDock [35]. The top scoring model docked at Site 2 and having the lowest energy was selected. In the final docked conformation, the peptide unfolded further at the termini and had a backbone rmsd of 3.5 Å from the initial docked position. The solvent accessible surface area buried due to peptide binding was 620 $Å^2$. In the docked position, the peptide was found to display similar interactions as those found between MoxX and MoxT at Site 2. A detailed view of the peptide-MoxT interactions is shown in Fig. 6. The backbone mimicked that of residues 44–49 of MoxX and can be seen superposed on the MoxXT complex (Fig. 6, inset). The main interacting residues of the peptide are Trp6, Ala7, and Ser8. Ile3 of the peptide interacts closely with Phe38 and Pro40 (MoxTb) and Ala5 of the peptide interacts with the side chains of Lys55 and Leu56 (MoxTa). The Trp6 side chain is buried in the hydrophobic interface between the MoxT monomers. It is surrounded by side chains of Leu56, Pro57, Thr58, and Glu78 (MoxTa) and Ile34, Phe38, Ser39, Pro40, and Thr41 (MoxTb). Ala7 of the peptide lies close to Ser19 (MoxTa) and Phe38, Ser39, Pro40 (MoxTb). Ser8 of the peptide was also surrounded by a number of polar side chains including Lys55, His59, Glu78 and by non polar Ile51 and Leu56 (MoxTa) and Pro40 (MoxTb).

In order to unequivocally demonstrate the direct ability of peptide to bind to rMoxT, ELISA and Blot overlay assay was performed. As is evident, a dose dependent decrease in the ability of MoxT to bind to peptide was observed (Fig. 7). This was also substantiated by Blot overlay assay, wherein, peptide was loaded on the gel and was overlaid with rMoxT. A specific band at 0.8 kDa corresponding to the peptide, depicted by an arrow, suggested that the rMoxT specifically interacted with the peptide (Fig. 7, inset b). Absence of any discernible immunoreactive band (Fig. 7, inset b, Lane 3) with BSA as the bait and rMoxT as the overlaid protein confirmed the specificity of rMoxT in binding to specific protein. A parallel coomassie stained gel, demonstrating the loaded peptide and BSA, is also shown in panel A of Fig. 7 (inset). Taken collectively, this provides direct proof of peptide binding to MoxT.

In vitro testing of the peptide concurred with the docking predictions and the peptide was efficacious at low micromolar concentration. It is emphasized that the peptide was tested for its ability to prevent the MoxXT complex formation rather than to disrupt the pre-formed complex. The ELISA studies showed that 2 μM of the designed

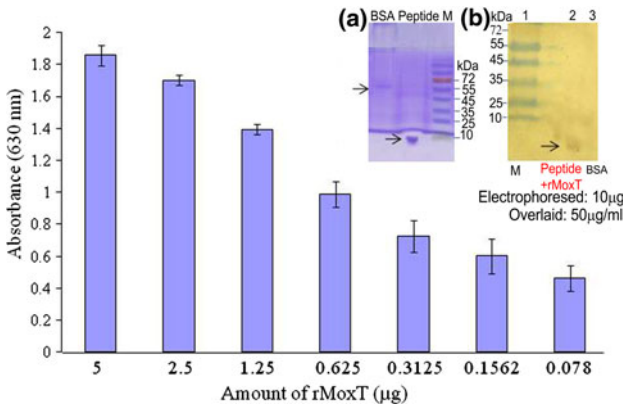


**Fig. 7** ELISA and Blot overlay assay of the designed peptide with rMoxT. The *bar* graph shows the absorbance observed with decreasing concentration of rMoxT. The *inset* shows (*a*) Gel electrophoresis: BSA and peptide (10 µg each). (*b*) Blot overlay: peptide and BSA overlaid with rMoxT (50 µg). The binding is depicted by an *arrow*. The graph was prepared using MS excel

peptide decreased the binding of MoxX to MoxT by 42%. In general, it is extremely difficult to inhibit protein–protein complex formation with the help of small peptides or organic molecules due to the magnitude of the surface area buried upon interaction. However, the TA complexes of the MazEF/PemIK family are uniquely suited for inhibition of complex formation since the antitoxin assumes an elongated state at the C-terminus that mediates binding to the toxin.

As mentioned before, the peptide was designed to bind to Site 2 of MoxT. Since Site 2 is the known ribonuclease binding site, therefore, it was speculated that the peptide interactions at this site could inhibit the RNA cleavage. Thus, the protective effect of peptide, if any, on the ribonuclease activity of MoxT was assessed. Firstly, as a

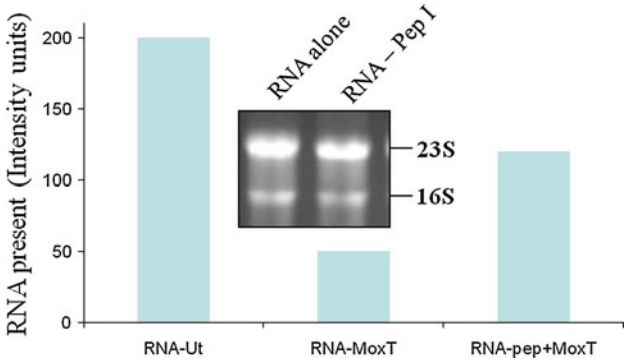


**Fig. 8** Peptide inhibition of Ribonuclease activity of MoxT. The untreated RNA and RNA-MoxT (5 µg) was added to a preincubated complex of 125 µM of the peptide and 20 µM MoxT (overnight at 4 °C) for 2 h at 37 °C. The percentage of intact/remaining RNA was quantitated by a densitometer (Bio-Rad) and plotted as intensity units. The RNA alone and RNA-MoxT was taken as positive control. The graph was plotted using MS Excel

control, the peptide alone was incubated with RNA to ascertain whether the peptide itself had the potential to degrade RNA. As expected, the peptide alone does not possess the ribonuclease activity and has no deleterious effect on RNA (Fig. 8). The peptide (125 µM) was then preincubated with 20 µM MoxT to facilitate its interaction with Site 2 followed by the addition of RNA. The assay showed partial inhibition of MoxT ribonuclease activity (Fig. 8), thus indicating that the peptide masks the active site of MoxT by binding at Site 2. A 15 amino acid long nonspecific random peptide and an 8 amino acid long *N*-terminal peptide had no effect on MoxT ribonuclease activity and degraded RNA to the same extent as the wild type MoxT, indicating the specificity of the interaction [7]. As there is only partial inhibition of the ribonuclease activity in presence of the peptide, therefore, it can be concluded that it is possible to interfere with MoxXT binding at Site 2 without completely inhibiting the MoxT ribonuclease activity. However, we speculate that designing more specific peptides that bind exclusively to Site 1 of MoxT will inhibit MoxX binding without interfering with the ribonuclease activity of MoxT. Thus, Site 1 specific peptides will theoretically be more potent in inducing programmed cell death within the host and can be exploited for the development of novel efficacious antianthrax drugs.

## Promoter elements are localized in the upstream region extending from −50 to −100

In order to identify transcription initiation sites in the upstream region of the MoxXT module, transcriptional fusions with a promoterless *lacZ* gene as a reporter were carried out. For this, the stepwise deletion fragments from the 5′ end of the upstream of the *moxX* gene were cloned in the promoterless *placZ* vector. The functionality of each fragment as a promoter was validated by assessing *β*-galactosidase activity and compared with cells transformed with control plasmid (only vector). The 50 bp fragment immediately upstream of the *moxX* ORF showed no activity. The maximal level of expression was obtained in a region of 100 bp upstream fragment (−100 to 0), as shown in Fig. 9. Interestingly, all the other fragments harboring the promoter were not able to drive the expression of *β*-galactosidase efficiently unlike the 100 bp (spanning −100 to 0). This could be attributed to the presence of uncharacterized negative regulatory *cis*-elements.

## MoxT increases DNA-binding ability of MoxX

We have previously shown that the recombinant(r) MoxX possessed the ability to bind to the upstream promoter region. As shown from deletion analysis of upstream region, there is a promoter region upstream of MoxXT

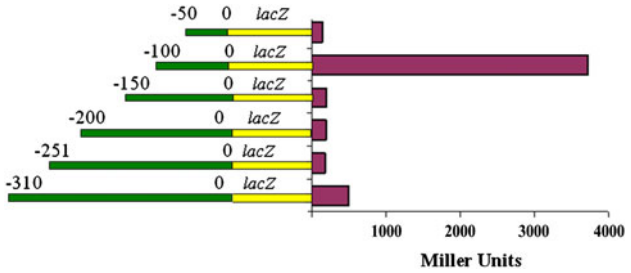


**Fig. 9** Transcriptional activation mediated by the upstream regulatory regions of MoxX. Schematic representations of various plasmids used in the reporter gene assay are given on the left. The plasmid drawings are not to the scale. Promoterless plasmid *placZ* containing *β*-galactosidase as the reporter gene was used as a control and several deletions from the 5′ end were fused upstream to this reporter gene. [The ability of each construct to drive the *β*-galactosidase expression was expressed as total miller units which are, 1000 × (Absorbance at 420 nm)/(Absorbance at 595 nm) × Time (20 min) × Volume (1 mL). The values represent mean of three values obtained from three independent experiments]

ORF extending from −50 to −100 and an additional regulatory region from −100 to −150. Therefore, in order to probe MoxXT binding, a 200 bp construct extending from 0 to −200 of the ORF was taken. We determined the concentration of MoxX required for binding to the DNA alone and in conjunction with MoxT. As is evident from Fig. 10, the rMoxX was incompetent to bind to the upstream regulatory regions at any concentration below 2 μM. However, it can clearly be seen that in a complex

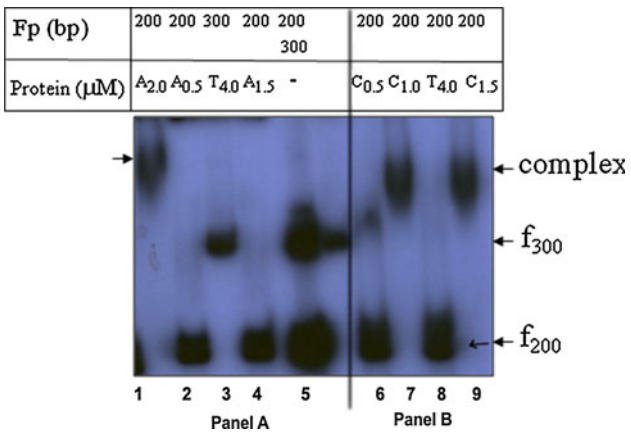


**Fig. 10** DNA binding ability of MoxX in presence of MoxT as shown by standard gel retardation assay. *Panel a* $F_{200}$ corresponds to the radiolabeled 200 bp fragment of the upstream region −50 to −250. $F_{200}$ with increasing concentrations of rMoxX (A), namely 0.5, 1.5 and 2.0 μM is shown in *lanes 2, 4* and *1*, respectively. It is evident that there is no binding of the rMoxX (A) to $F_{200}$ below concentrations of 2.0 μM. *Lane 3* shows that there is no complex formation of rMoxT (T) alone with $F_{300}$ (the total promoter) even at 4.0 μM. *Lane 5* corresponds to the $P^{32}$ labeled free probes, $F_{200}$ and $F_{300}$ run simultaneously. *Panel b Lanes 6, 7 and 9* represent appearance of high molecular weight species (C/Complex) with 0.5 μM, 1.0 μM and 1.5 μM rMoxX in the presence of 1 μM rMoxT. *Lane 8* corresponds to 4.0 μM of rMoxT with $F_{200}$

containing rMoxT (1 μM), the concentration of rMoxX required to bind to DNA fell down substantially (from 2 to 0.5 μM). The complex, therefore, produced a slower migrating species at a four-fold lower protein concentration than that generated by rMoxX alone in a standard gel retardation experiment. The intensity of the complex formed did not increase upon increasing in MoxT concentration from 1 to 1.5 μM (Fig. 10, depicted as $C_{1.0}$–$C_{1.5}$). This indicates that the maximal complex formation is achieved at a molar ratio of 1:1. This is in concordance with our stoichiometry data that assigns a 1:1 stoichiometry for the rMoxXT interaction [7]. However, the rMoxT alone failed to interact with DNA (Fig. 10, lanes 3 and 8) with either of the fragment(s) at even four times the concentration used (4 μM). This indicates a more proficient binding of MoxXT complex (possessing equimolar ratios of rMoxT and rMoxX) to the promoter regions as compared to rMoxX alone. Taken together with its repressor action and increase in its DNA-binding affinity, MoxX and MoxT can form a repressor-corepressor pair. There could be several explanations or possibilities for this, namely: (a) a high degree of cooperativity in regulation, (b) stabilization of the rMoxX-DNA complex at the operator site by toxin or (c) stabilization of the rMoxX upon binding to the rMoxT followed by structural perturbation and formation of a stable conformation which might permit improved DNA binding.

## Palindromic sequences in upstream DNA constitute the MoxX binding site

We have already shown that MoxX recognizes and binds to DNA alone and in conjunction with MoxT. It has also been established that this is accomplished by binding to the upstream region from −50 to −100 from the start codon of *moxX*. Therefore, the upstream region 0 to −100 was scanned for repressor elements and was found to harbor a perfect short palindrome (SP) 5′-TTGCAA-3′ (−83 to −88), which could act as recognition elements for the MoxX RHH motif. On comparison of operator sequences of CcdAB [15], RelBE [16], FitAB [43], *ωεζ* [44] TA modules, and NikR-operator DNA [17] sequences, wherein the transcriptional repressor proteins have a RHH binding motif, it was observed that the RHH proteins bind to DNA in a sequence specific manner. The CcdA antitoxin brings about autorepression by binding to a 6 bp palindrome 5′-GTATAC-3′ in the operator region. RelB binds to hexad direct repeats and inverted repeats with the palindromic consensus sequence 5′-TT(G/A)(T/C)AA-3′ in the operator region. Additionally, an imperfect long palindrome (LP) 5′-TACAATGGTA-3′ was observed upstream of MoxX at the position −72 to −63. Similar TA binding imperfect palindromes 5′-TGCTATCA-3′ were observed upstream of

*fitAB* operon. Further mutating the palindrome to a perfect one led to 1.5 fold enhancement of DNA-binding affinity [18]. The $\omega$ antitoxin is seen as an exception wherein binding takes place to divergent pseudo/non-palindromic DNA heptads with the consensus sequence 5′-(A/T)ATCAC(A/T)-3′. Further, it has been observed that there may be many subsites available in the operator/promoter region for antitoxin interaction and that the affinity of binding of the antitoxin to these sites differs. To establish a direct involvement of these short and long palindromes in MoxX binding, ethidium bromide displacement assay was performed.

As is evident from Fig. 11 (Panel a), rMoxX was found to interact with DNA containing both the motifs (LP + SP). A decrease in relative fluorescence intensity (RFI) of EtBr was obtained after rMoxX addition, indicating DNA binding. The nonspecific DNA (30 bp) with the rMoxX and nonspecific protein (BSA) with the specific DNA employed in the present study, did not cause a decrease in the RFI, indicating a specific binding of the DNA with rMoxX (Fig. 11, Panel b). This establishes that both or either of the palindromes (LP and SP) is implicated in binding to MoxX, thus pointing to a common recognition mechanism facilitating autoregulation in RHH containing antitoxins. The hexad perfect palindrome observed at −83 to −88 upstream to MoxX is also consistent with the presence of regulatory elements in the region extending from −50 to −100 as determined by LacZ expression assay. The sequence 5′-TTGCAA-3′ is similar to the consensus motif, 5′-TT(G/A)(T/C)AA-3′ established in the RelBE operator sequence. Previously, higher affinity of RHH motif binding to DNA has been observed with palindromic regions [16]. Binding of MoxX to an oligomer containing the hexad has also been established. Thus, the DNA sequence containing the perfect palindrome 5′-TTGCAA-3′ was used for modeling the MoxX-DNA complex.

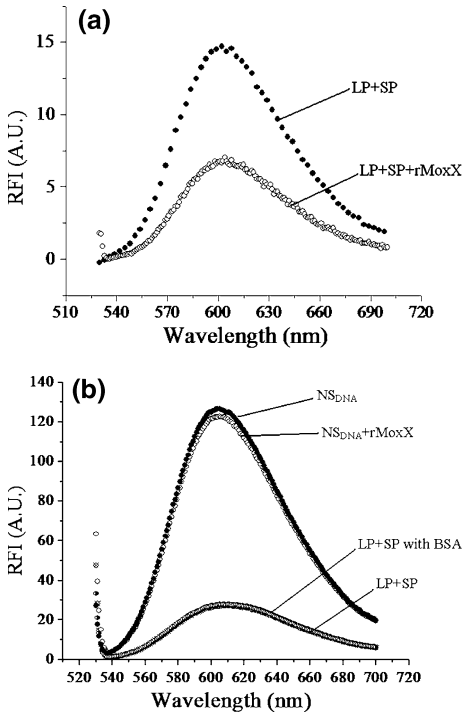


**Fig. 11** The potential of the rMoxX to bind to palindromic motifs located upstream in the regulatory regions of the operon using EtBr displacement assay. DNA–protein interaction **a** The EtBr displacement assay was performed in the presence of the rMoxX and LP + SP (long palindrome: TACAATGGTA, short palindrome: TTGCAA). The interaction of the DNA with the rMoxX was performed at 25 °C for 1 h. **b** Determination of the specificity of interaction: The DNA binding potential of the rMoxX was assessed using fluorescence spectroscopy as described. The decrease in the fluorescence emission of EtBr upon nonspecific random DNA sequence-rMoxX interaction and specific DNA (LP + SP) with BSA as a nonspecific protein is depicted. The RFI values were plotted using Cary eclipse software

## MoxX binds to DNA by insertion of ribbon in the major groove: specific conserved interactions mediating recognition

The 6 bp perfect palindromic nucleotide sequence determined by us as the probable DNA-binding region was modeled as B-form DNA on the basis of CcdA bound DNA template (PDB ID: 2H3A) [15], which contains a perfect palindromic sequence 5′-GTATAC-3′. The complex was formed by superposition on NikR-DNA complex. The modeled MoxX-DNA complex was subjected to MD simulations.

MoxX binds to DNA by insertion of its ribbon into the DNA major groove as shown in Fig. 12. Specific recognition of the 5′-TTGCAA-3′ palindrome by MoxX is mediated by interactions with its ribbon residues 8–13. MoxXb Glu9 backbone interacts with the backbone of T2′-O2P. There are also extensive hydrophobic interactions of side chains of Ile10 and Val11 of MoxX with bases T1′ and T2′. These interactions position the MoxX RHH domain over the DNA such that there are base specific contacts with MoxXa and MoxXb Arg13 in the major groove. The guanidium group of Arg13 of MoxXa forms hydrogen bonds with DNA:3T-O4 while Arg13 of MoxXb forms hydrogen bonds with O4 of T1′. MoxXa Arg13 also forms hydrogen bonds with O6 of G4. MoxXb Glu9 interacts with T2′-C7, G3′-C4 and C4′-N4. Apart from the ribbon residues of MoxX, backbone interactions involving MoxXb:33Arg-N and 3T′-O2P are observed. The guanidium group of Arg33 of MoxXb forms hydrogen bonds with DNA:3T-O2P. Additional hydrogen bonding is also seen between MoxXb:33Arg-HH11 and DNA:4G-O2P as well as MoxXb:33Arg-HH21 and DNA:4G-O2P.

We compared these interactions with those found in CcdA-operator DNA structure as well as the modeled

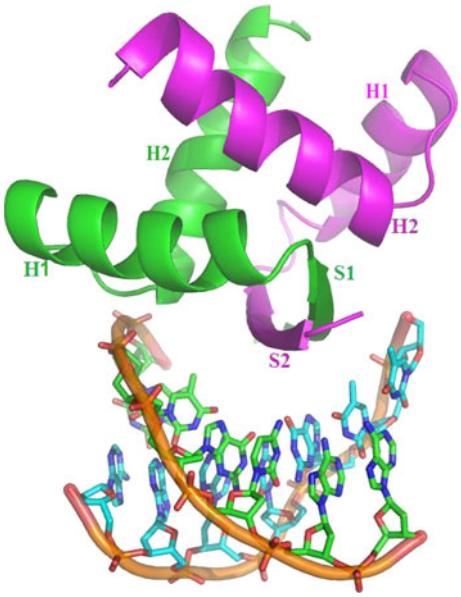


**Fig. 12** MoxX-DNA complex. The DNA is shown as *orange* colored ribbon with the bases rendered as sticks. The two MoxX chains are shown in *green* and *magenta* with the secondary structure elements labeled. The figure was rendered using Pymol

ParD-DNA structure and found them to be similar. In CcdA-DNA solution structure, Arg4 and Thr6 of the antitoxin are found to make critical contacts with the DNA, while in ParD-DNA complex, Arg3 and Thr5 are found to be involved in DNA recognition and binding. On sequence/structural alignment of the *N*-terminal residues of CcdA and ParD with the RHH motif of MoxX, we found that the Val11 residue of MoxX is involved in making interactions with DNA. This corresponds to Thr5 in CcdA and Thr6 in ParD respectively, which also make similar interactions with DNA. Also, the sequence alignment shows that in MoxX, Glu9 occupies the position which is occupied by Arg in ParD/CcdA. Arg13 in MoxX, which is involved in numerous contacts with DNA, is aligned with Asp residue in ParD/CcdA. Conserved Arg and hydrophobic residues such as Thr/Val in the RHH motif are found to be involved in recognition and binding of the DNA in the major groove in the antitoxins CcdA, ParD, and MoxX. The occurrence of specific hexad recognition elements in DNA combined with conserved protein interactions point to a common mode of binding and interaction of RHH family antitoxins with DNA. Therefore, our future structure based design strategy will revolve around identifying compounds to disrupt these specific interactions.

## Conclusion

Deletion mutant studies have established that MoxX binds to its cognate toxin MoxT via its extended *C*-terminal region and to its upstream operator DNA by the *N*-terminal RHH region. We have used clues from functional studies on deletion mutants to model MoxX in complex with MoxT and its cognate upstream DNA. The structure of MoxXT has been further validated by the design of a peptide that could inhibit MoxX binding to MoxT. In addition to providing valuable insight into the structure and mechanism of MoxXT, the two models reported here will facilitate rational design of chemical moieties to disrupt the MoxX interaction with MoxT or its upstream regulatory region. Both these strategies have the potential of unleashing the activity of MoxT as a novel antibacterial agent. This is also important in view of the widespread occurrence of this family of TA modules in bacteria, and emerging issues of multidrug resistance.

**Acknowledgments** Authors would like to acknowledge Prof. B. Jayaram for providing access to Super Computing Facility for Bioinformatics and Computational Biology, IIT (Delhi) for running MD simulations. We also acknowledge the help of Barak Raveh and Ora Schueler-Furman at the Hebrew University, Jerusalem for enabling exhaustive runs of FlexPepDock simulations on their server and for their valuable inputs. N.C. acknowledges University Grants Commission and Council of Scientific and Industrial Research for providing financial assistance.

## References

1. Jensen RB, Gerdes K (1995) Programmed cell death in bacteria: proteic plasmid stabilization systems. Mol Microbiol 17:205–210
2. Gerdes K, Christensen SK, Lobner-Olesen A (2005) Prokaryotic toxin-antitoxin stress response loci. Nat Rev Microbiol 3:371–382
3. Gerdes K, Rasmussen PB, Molin S (1986) Unique type of plasmid maintenance function: postsegregational killing of plasmid-free cells. Proc Natl Acad Sci USA 83:3116–3120
4. Aizenman E, Engelberg-Kulka H, Glaser G (1996) An E. coli chromosomal 'addiction module' regulated by guanosine 3′–5′-bispyrophosphate: a model for programmed bacterial cell death. Proc Natl Acad Sci USA 93:6059–6063
5. Brooun A, Songhua L, Lewis K (2000) A dose-response study of antibiotic resistance in *Pseudomonas aeruginosa* biofilms. Antimicrob Agents Chemother 44:640–646
6. Agarwal S, Agarwal S, Bhatnagar R (2007) Identification and characterization of a novel toxin-antitoxin module from *Bacillus anthracis*. FEBS Lett 581:1727–1734
7. Agarwal S, Mishra NK, Bhatnagar S, Bhatnagar R (2010) PemK toxin of *Bacillus anthracis* is a ribonuclease: an insight into its active site, structure and function. J Biol Chem 285:7254–7270
8. De Jonge N, Garcia-Pino A, Buts L, Haesaerts S, Charlier D, Zangger K, Wynes L, De Greve H, Loris R (2009) Rejuvenation of CcdB-poisoned gyrase by an intrinsically disordered protein domain. Mol Cell 35:154–163
9. Oberer M, Zangger K, Gruber K, Keller W (2007) The solution structure of ParD, the antidote of the ParDE toxin–antitoxin module, provides the structural basis for DNA and toxin binding. Protein Sci 16:1676–1688
10. Raumann BE, Rould MA, Pabo CO, Sauer RT (1994) DNA recognition by $\beta$-sheets in the Arc repressor-operator crystal structure. Nature 367:754–757

11. Gomis-Ruth FX, Sola M, Acebo P, Parraga A, Guasch A, Gonzalez EritigaR, Espinosa M, del Solar G, Coll M (1998) The structure of plasmid-encoded transcriptional repressor CopG unliganded and bound to its operator. EMBO J 17:7404–7415
12. Somers WS, Philips SE (1992) Crystal structure of the met repressor-operator complex at 2.8 Å resolution reveals DNA recognition by $\beta$-strands. Nature 359:387–393
13. Schreiter ER, Sintchak MD, Guo Y, Chivers PT, Sauer RT, Drennan CL (2003) Crystal structure of the nickel-responsive transcription factor NikR. Nat Struct Biol 10:794–799
14. Kamada K, Hanoaka F, Burley SK (2003) Crystal structure of MazE/MazF complex: molecular bases of antidote-toxin recognition. Mol Cell 11:875–884
15. Madl T, Melderen VM, Mine N, Respondek M, Oberer M, Keller W, Khatai L, Zangger K (2006) Structural basis for nucleic acid and toxin recognition of the bacterial antitoxin CcdA. J Mol Biol 364:170–185
16. Li GY, Zhang Y, Inouye M, Ikura M (2008) Structural mechanism of transcripitional autorepression of the *E. coli* RelB/RelE antitoxin/toxin module. J Mol Biol 380:107–119
17. Schreiter ER, Wang SC, Zamble DB, Drennan CL (2006) NikR-operator complex structure and the mechanism of repressor activation by metal ions. Proc Natl Acad Sci USA 103:13676–13681
18. Mattison K, Wilbur JS, So M, Brennan RG (2006) Structure of FitAB from *Neisseria gonorrhoeae* bound to DNA reveals a tetramer of toxin-antitoxin heterodimers containing pin domains and ribbon-helix-helix motifs. J Biol Chem 281:37942–37951
19. Kedzierska B, Lian L, Hayes F (2007) Toxin–antitoxin regulation: bimodal interaction of YefM–YoeB with paired DNA palindromes exerts transcriptional autorepression. Nucleic Acids Res 35:325–339
20. Gogos A, Mu H, Bahna F, Gomez CA, Shapiro L (2003) Crystal structure of YdcE protein from *Bacillus subtilis*. Proteins 53:320–322
21. Andrade MA (1993) Evaluation of secondary structure of proteins from UV circular dichroism spectra using an unsupervised learning neural network. Protein Eng 6:383–390
22. Fiser A, Do RK, Sali A (2000) Modeling of loops in protein structure. Protein Sci 9:1753–1773
23. Laskowski RA, MacArthur MW, Moss DS, Thornton JM (1993) PROCHECK: a program to check the stereochemical quality of protein structures. J Appl Crystallogr 26:283–291
24. Marchler-Bauer A, Anderson JB, Chitsaz F, Derbyshire MK, DeWeese-Scott C, Fong JH, Geer LY, Geer RC, Gonzales NR, Gwadz M, He S, Hurwitz DI, Jackson JD, Ke Z, Lanczycki CJ, Liebert CA, Liu C, Lu F, Lu S, Marchler GH, Mullokandov M, Song JS, Tasneem A, Thanki N, Yamashita RA, Zhang D, Zhang N, Bryant SH (2009) CDD: specific functional annotation with the Conserved Domain Database. Nucleic Acids Res 37:D205–D210
25. Kelly LA, Sternberg MJE (2009) PHYRE:Protein structure prediction on the web: a case study using the PHYRE server. Nat Protoc 4:363–371
26. Söding J (2005) Protein homology detection by HMM-HMM comparison. Bioinformatics 21:951–960
27. Hall TA (1999) BIOEDIT, a user-friendly biological sequence alignment editor and analysis program for Windows 95/98/NT. Nucleic Acids Symp Ser 41:95–98
28. Arnold K, Bordoli L, Kopp J, Schwede T (2006) The SWISS-MODEL workspace: a web-based environment for protein structure homology modeling. Bioinformatics 22:195–201
29. Guex N, Peitsch MC (1997) SWISS-MODEL and the Swiss-PdbViewer: an environment for comparative protein modeling. Electrophoresis 18:2714–2723
30. Tovchigrechko A, Vakser IA (2006) GRAMM-X public web server for protein-protein docking. Nucleic Acids Res 34:W310–W314
31. Pearlman DA, Case DA, Caldwell JW, Ross WS, Cheatham TE III, DeBolt S, Ferguson D, Seibel G, Kollman P (1995) AMBER, a package of computer programs for applying molecular mechanics, normal mode analysis, molecular dynamics and free energy calculations to simulate the structural and energetic properties of molecules. Comput Phys Commun 91:1–41
32. Darden T, York D, Pederson L (1993) Particle Mesh-Ewald method: an N-log (N) method for ewald sums in large systems. J Chem Phys 98:10089–10092
33. Fung HK, Welsh WJ, Floudas CA (2008) Computational de novo peptide and protein design: rigid templates versus flexible templates. Ind Engin Chem Res 47:993–1001
34. Maupetit J, Derreumaux P, Tuffery P (2009) PEP-FOLD: an online resource for de novo peptide structure prediction. Nucleic Acids Res 37(suppl 2):W498–W503
35. Raveh B, London N, Schueler-Furman O (2010) Sub-angstrom modeling of complexes between flexible peptides and globular proteins. Proteins 78:2029–2040
36. Cutting SM, Vander Horn PB (1990) Genetic analysis. In: Harwood CR, Cutting SM (eds) Molecular biological methods for Bacillus. Wiley, UK, pp 27–74
37. Van Dijk M, Bonvin AM (2009) 3D-DART: a DNA structure modeling server. Nucleic Acid Res 37:W235–W239
38. Schlessinger A, Punta M, Yachdav G, Kajan L, Rost B (2009) Improved disorder prediction by combination of orthogonal approaches. PLoS One 4:e4433
39. Kamphuis MB, Monti MC, van den Heuvel RH, López-Villarejo J, Díaz-Orejas R, Boelens R (2007) Structure and Function of bacterial Kid-Kis and related toxin-antitoxin systems. Protein Pept Lett 14:113–124
40. Chivers PT, Tahirov TH (2005) Structure of *Pyrococcus horikoshii* NikR: nickel sensing and implications for the regulation of DNA recognition. J Mol Biol 348:597–607
41. Dian C, Schauer K, Kapp U, McSweeney SM, Labigne A, Terradot L (2006) Sructural basis of the nickel response in Helicobacter pylori: crystal structures of HpNikR in Apo and nickel bound states. J Mol Biol 361:715–730
42. Ananthraman V, Aravind L (2003) New connections in the prokaryotic toxin-antitoxin network: relationship with the eukaryotic nonsense-mediated RNA decay system. Genome Biol 4:R81
43. Wilbur JS, Chivers PT, Mattison K, Potter L, Brennan RG, So M (2005) *Neisseria gonorrhoeae* FitA interacts with FitB to bind DNA through its ribbon-helix-helix motif. Biochemistry 44:12515–12524
44. Weihofen WA, Cicek A, Pratto F, Saenger W (2006) Structures of omega repressors bound to direct and inverted DNA repeats explain modulation of transcription. Nucleic Acids Res 34:1450–1458